Thermal behavior of indium nanoclusters in ion-implanted silica

M. A. Tagliente,[1,*] G. Mattei,[2] L. Tapfer,[1] M. Vittori Antisari,[1] and P. Mazzoldi[2]

[1]*ENEA, CR Brindisi, UTS MAT-COMP, SS.7 Appia km 714, I-72100 Brindisi, Italy*
[2]*INFM-Dip. di Fisica, Università di Padova, via Marzolo 8, I-35131, Padova, Italy*
(Received 17 October 2003; revised manuscript received 7 April 2004; published 31 August 2004)

Fused silica substrates were implanted with 2×10^{17} In^{2+}/cm^2 ions at 320 keV. Indium crystalline nanoclusters with an average size of about 15–20 nm were found in the as-implanted samples. The thermal behavior of the nanoclusters was studied by performing heating-cooling cycles in vacuum and by using *in-situ* techniques based on glancing-incidence x-ray diffraction and transmission electron microscopy. The precipitates showed both superheating and supercooling. Moreover, no evidence of clusters growth or reorientation during the thermal cycle was found. A detailed study of the heating sequence showed that the melting temperature of the Indium precipitates depended on their size, i.e., the smallest particles melt first and at a temperature which is about 7 K below the bulk melting point, while the largest ones were superheated until about 13 K above it. Moreover, a remarkable stability of the In cluster well above their melting temperature (up to about 980 K) was evidenced by *in-situ* transmission electron microscopy analysis. From a thermodynamic point of view, the experimental results were explained by considering two effects acting on the clusters: the thermodynamic size effect and the pressure of the silica matrix.

I. INTRODUCTION

The great interest toward clusters of atoms with nanoscopic size is due to both fundamental and technological reasons. From a fundamental point of view, the low number of atoms forming the cluster and the relevant fraction of atoms on the cluster surface make them intrinsically different from either the bulk phase or the atomic state in terms of physical and chemical properties, such that somebody speaks of a new state of the matter.[1–8] The peculiar properties involve the electronic band structure, the structural configuration, the value of the lattice parameter and thermodynamic properties such as the melting point, vapor pressure and so on.

Moreover, if the clusters are embedded in dielectric matrices, their interaction with external fields leads to peculiar responses. In particular, metallic nanoclusters (NCs) embedded in glass can increase the optical third-order susceptibility of the composite by several orders of magnitude.[4]

On the other hand, the technological interest is related to the possibility of exploiting the peculiar properties for application purposes in different fields such as catalysis,[9] optoelectronic,[10–13] and magnetic information storage.[14] Since these properties depend on various different parameters (such as, for example, cluster size distribution, shape and composition, cluster-matrix interaction), in principle the physical properties of the nanostructured systems can be finely tuned and tailored for obtaining materials with predefined characteristics.

Among different synthesis techniques, ion implantation in glass is very effective to obtain tailored nanostructured composites by varying the implantation conditions (energy, and ion fluence, as well as substrate temperature) and performing post-implantation annealings.[15–18]

The need of controlling the nanoclusters properties during the synthesis process or the post thermal annealing has induced several structural studies.[18–22] Of particular relevance both from a technological and a fundamental point of view are the studies about the thermal behaviors of nanostructured systems.[21–30] A comprehensive understanding of the thermal behavior is crucial because it is directly related to the stability, structure and size of the clusters.

Thermodynamically, it is well known that the melting point T_m of a small cluster with free surface, that is an isolated cluster in vacuum, is lower than that of the infinite bulk solid.[30] This can be understood according to phenomenological models in which the Gibbs energy of the system has an additional term with respect to the bulk accounting for the free energy at the cluster surface. On the other hand, for clusters without free surface, i.e., embedded in a matrix, many experimental and theoretical works suggest that the embedded clusters can achieve superheating (or melting point elevation) and supercooling (or solidification point elevation).[21,23,24,27] Inclusions of lead in implanted aluminium single crystals with an average size of 14 nm showed a superheating of 67 K and a supercooling of 21 K with respect to the bulk melting point, indicating the presence of an hysteresis cycle.[21] Indium particles with average radius of 4 nm embedded in implanted (110) aluminum single crystals exhibited superheating of 23 K and supercooling of 21 K.[27] Molecular dynamics simulations for embedded lead clusters indicated that the clusters can be superheated.[24] Generally, the superheating has been addressed to the depressed mean square amplitude of vibration of atoms at the interfaces with respect to the atoms of the interior of the cluster if the host matrix has a higher melting point.[31] Moreover, it was found that coherent or semicoherent interfaces between the clusters and the matrix were necessary to obtain superheating.[32] It was also reported that in this case the change in T_m of the superheated clusters is size dependent and proportional to the inverse size of the embedded clusters, with the consequence that the smaller the cluster, the higher T_m.[24]

Moreover, during annealing of clusters embedded in a matrix, a significant growth can be also observed, due to growth mechanisms such as loop punching,[33] Ostwald ripening[34] and coalescence of inclusions.[35]

In this work, we report on the results about the melting-solidification behavior and the thermal stability of Indium (In) nanoclusters embedded in silica. The investigated In-silica composite was produced by ion implantation, while the characterization was carried out by glancing incidence x-ray diffraction (GIXRD) and transmission electron microscopy (TEM). The reason for our interest toward this material is twofold: (i) the fact that In, having a low melting point (429.8 K), offers the possibility to investigate very easily the thermal behavior of nanometric clusters embedded in a matrix; and that (ii) the implantation of In clusters in silica is the first step of the synthesis of In-based binary semiconductor compounds (InN, InP) by sequential ion implantation.

II. EXPERIMENTAL PROCEDURE

Fused silica (type II, Heraeus) slides were implanted with an In^{2+} ion beam by using a high current Ion Implanter DANFYSIK 1090 at normal incidence. Implantations were performed at room temperature and the current densities were maintained lower than 2 $\mu A/cm^2$, in order to avoid possible heating during the implants. The implantation conditions, 320 keV energy and 2×10^{17} In^{2+}/cm^2 ion dose, were chosen to have a subsurface buried layer of In nanoprecipitates of some tens of nanometers thick (the calculated ion projected range Rp is about 100 nm with a straggling ΔRp = 70 nm).

After the implantation, the samples were subjected to thermal cycles during which the structural properties of In clusters were studied by means of *in-situ* GIXRD and TEM. GIXRD experiments were carried out by using a Philips MPD PW1880 x-ray diffractometer in parallel beam geometry by employing CuK_α radiation (λ_{CuK_α}=0.154 186 nm) and equipped with a temperature chamber (ANTON PAAR). During the measurements, the incident x-ray beam was fixed at a small angle of incidence (typically 0.5°, which corresponds to a penetration depth of 280 nm in silica[36]) while the detector was moved along the goniometer circle in a defined 2θ range. Sample heating was provided by mounting the sample on the copper base of a small furnace which could be operated in the temperature interval 80–575 K. The temperature was measured by using a Pt 100 thermocouple embedded in the copper base and precisely controlled (± 0.1 K). A low vacuum condition (pressure of 10^{-3} torr) was reached in the chamber using a rotatory pump. The x-ray diffraction from In inclusions was studied through a heating and cooling sequence from room temperature (RT) to 453 K and back by measuring the (101)In reflection in the 2θ range 31°–35°. During the cycle, the sample was thermalized for 60 min, then the In(101) peak was scanned at a fixed temperature and the scan lasted 30 min.

TEM analysis has been performed on cross-sectional samples with a Philips CM30T microscope at CNR-IMM Institute (Bologna, Italy) operating at 300 kV and equipped with heatable sample holder (Gatan model 652 double tilt)

with a type R thermocouple spot welded to the heater tantalum body of the furnace allowing a maximum sample temperature of 1200 K. Thermalization of the sample at each temperature has been obtained with 15–20 min time intervals. After the thermalization, bright-field (BFTEM) images and selected-area electron diffraction (SAED) patterns have been recorded. Two *in-situ* TEM experiments were carried out: (i) a first thermal cycle was from RT up to 453 K and back to RT to evidence the possible hysteretic behavior of the melting-solidification process; (ii) then a second thermal sequence from RT up to 973 K was performed to investigate the stability of the clusters well above the melting temperature.

III. X-RAY DIFFRACTION METHOD

The shape of a diffraction peak from a system of small crystalline clusters is the convolution of functions representing the finite size of the coherent domains and the lattice defects. In practical cases, the clusters do not have the same size and the peak shape is also affected by the size distribution, and so it would be considered as a sum of the different contributions. As a consequence, it should be possible to extract information about size distribution and shape of the clusters through a careful analysis of the diffraction peak profile. In the following we will consider only size effects. The diffraction line profile $I(2\theta)$ at the Bragg angle 2θ from a small crystal of arbitrary shape is given by[37]

$$I(2\theta) = \frac{\cos\theta}{\lambda} I(s), \tag{1}$$

where λ is the x-ray wavelength and $I(s)$ is the intensity in reciprocal space expressed as a function of the distance s from the nearest reciprocal space point (hkl),

$$I(s) = \frac{\int_{-\tau}^{+\tau} V(t)\cos(2\pi st)dt}{U}, \tag{2}$$

where U is the volume of the unit cell. $V(t)$, the Fourier transform of $I(s)$, can be conveniently represented as the volume common to the crystal and its "ghost" shifted a distance t in the direction of the diffraction vector, and the limits of integration are the positive and negative values of t for which $V(t)$ vanishes. The explicit form of $I(s)$ for spherical crystals has been derived by Langford and Wilson,[38]

$$I(s) = \frac{\pi D^4}{8}\{\psi^{-2} - \psi^{-3}\sin(2\psi) + \psi^{-4}[1 - \cos(2\psi)]\}, \tag{3}$$

where D is the diameter and $\psi = \pi s D$. The apparent crystal size ε_β, that is the volume-weighted average of the thickness of the crystal measured in the direction of the diffraction vector, is the reciprocal of the integral breadth β_s of $I(s)$ according to the Scherrer equation,[39]
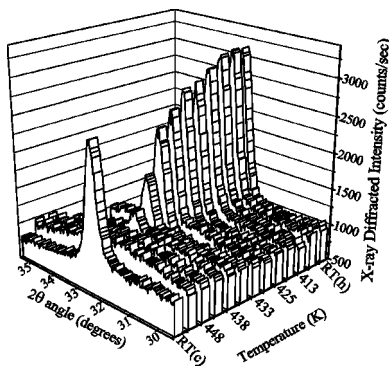
FIG. 1. X-ray diffraction scans collected around the In(101) peak and performed at the following temperatures (from right to the left): T=RT(h), 373, 413, 423, 425, 430, 433, 436, 438, 443, 448, 453 K and again at RT(c), after the cooling of the sample.

$$\varepsilon_\beta = \frac{\lambda}{\beta \cos \theta},\qquad(4)$$

where β is the integral breadth of the $I(2\theta)$ profile. The volume averaged true size $\langle Dv \rangle$ defined as the cube root of the crystallite volume is given by

$$\langle Dv \rangle = K\varepsilon_\beta,\qquad(5)$$

where K is the Scherrer constant which depends on the crystal shape. In the case of spherical clusters, $\langle Dv \rangle$ represents the volume-weighted mean diameter and $K=4/3$.

Diffraction line profiles from a system of clusters with a distribution of crystallite size can be calculated by summing $I(s)$, weighted by a function of the sizes distribution, for a particular morphology. For a log normal size distribution and spherical crystallites, diffraction line profiles are given by[39]

$$Y(s) = \frac{\int I(s,D) d\Lambda(D)}{\int \frac{\pi D^3}{6} d\Lambda(D)}\qquad(6)$$

with

$$d\Lambda(D) = \frac{1}{D\omega\sqrt{2\pi}} \exp\left[-\frac{(\ln D - \gamma)^2}{2\omega^2}\right] dD,\qquad(7)$$

where γ and ω are the log normal mean and variance, from which several features of the distribution can be derived such as area- and volume-weighted mean, the arithmetic mean and the variance of the distribution.[39]

IV. EXPERIMENTAL RESULTS

Figure 1 shows the evolution of the In(101) x-ray diffraction peak during the heating sequence from RT to 453 K of the thermal cycle and after the cooling of the sample at RT. At RT, a clearly resolved (101) peak of the In tetragonal phase (Space Group I4/mmm No.=39, a=b=0.3252 nm, c=0.4946 nm, ICDD card No. 5-642) is clearly visible, that indicates the presence of In nanoscopic crystalline aggre-
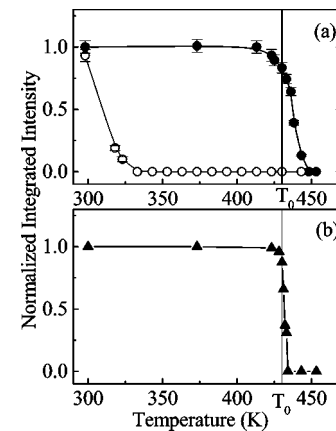

FIG. 2. (a) Normalized integrated intensity of the nanoclusters In (101) GIXRD peak versus the temperature for the thermal cycle between RT and 453 K. Solid and open circles represent data obtained during the heating and cooling sequences, respectively. The solid line connecting the experimental points is only a guide for the eye. The vertical solid line at T_0 indicates the In bulk melting point. (b) Normalized integrated intensity of a In film evaporated on a glass substrate, as comparison. The vertical solid line at T_0 indicates the In bulk melting point.

gates in the silica matrix in the as-implanted sample. When the temperature was raised until 413 K, the crystalline nature of indium clusters remains identical. In fact, we can observe that the diffraction peak remains unchanged until a temperature of about 413 K, after that it decreases in intensity. As the temperature was increased to 433 K, the indium diffraction peak was still present and diffuse scattering is clearly visible near the peak. The peak is measurable until 443 K, after that it disappeared accompanied by a broad diffuse scattering band in the vicinity of the peak, indicating a completely molten state.

Figure 2(a) shows the x-ray integrated intensity versus the temperature during the heating and the cooling sequences. Here, it is possible to see more clearly that during the heating sequence, superheating was observed up to 443 K, which is 13 K above the In bulk melting point T_0. During the cooling sequence, the solidification begins at 323 K, which is 107 K below T_0 (supercooling). After the recovery of the sample at RT, the integrated intensity was little decreased indicating only a small diffusion of the In atoms in the matrix. By repeating the thermal cycle, the same experimental results were found. Moreover, the measurement of the whole diffraction range excluded the possibility that the variation of the (101) diffraction peak was due to a reorientation of the clusters into a direction different from the (101).

To test the stability of the superheated and supercooled phases, the sample was kept at 433 K in the heating sequence and at 343 K in the cooling sequence for a week-end, each one. During these tests, the superheated and supercooled phases remained unaltered. To our opinion, these experimental results give unambiguous evidence of the presence of a thermal hysteresis loop across the melting and the solidification transitions of In clusters. Both superheating and supercooling are intrinsic physical phenomena. Last, in order to dissipate any doubt about the temperature measure-
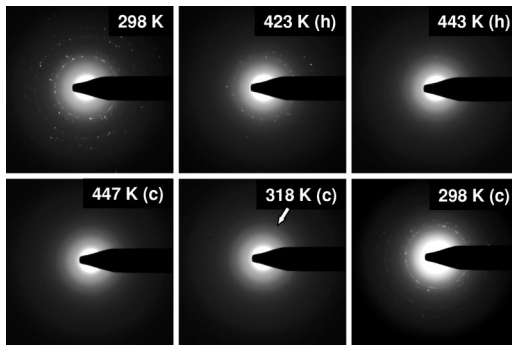
FIG. 3. SAED patterns showing the evolution of the electron diffraction from In clusters during the thermal cycle. The patterns were collected at the temperatures of 298 K (RT), 423 K, and 443 K during the heating sequence (label "*h*") and at 447 K, 318 K, and 298 K (RT) during the cooling sequence (label "*c*"). The white arrow indicates a crystalline spot in the diffraction pattern in the cooling cycle at 318 K (onset of recrystallization).

ments and the kinetic of the thermal cycle, we have checked the furnace by measuring the melting temperature of a thick In film evaporated on a glass substrate [Fig. 2(b)]. We found that the film definitely melted at 433 K which is 3 K higher than T_0: we ascribe this to the presence of small grains in the polycrystalline film. Indeed, as will be shown later, the superheating phenomenon is inversely related to the cluster size according to a surface effect. The trend of the In(101) integrated intensity of the film was added in Fig. 2, for comparison.

To directly follow the evolution of the In clusters during *in-situ* annealing, the same samples were investigated by TEM analyzing not only the hysteresis cycle but also extending the analysis well above the In melting temperature to study the thermal stability of the clusters. As far as the thermal cycle from RT up to 473 K is concerned a perfect agreement with the XRD results is obtained. Figure 3 shows some SAED patterns showing the evolution of the electron diffraction in the thermal cycle from RT up to 453 K (heating) and back to RT (cooling). Here, it is evident that in the heating sequence (labelled by "*h*" in Fig. 3) some crystalline spots are present up to 443 K and after that temperature, there is the complete disappearing of any spot (a completely molten state) in quantitative agreement with XRD results. On the other hand, in the cooling sequence (labelled by "*c*") the first crystalline spots appear only at 318 K and a complete recrystallization of the clusters is obtained at RT. This confirms the presence of a hysteresis cycle which clearly separates the melting and solidification temperatures. Moreover the quantitative agreement between TEM and XRD in terms of the transition temperatures (superheating and supercooling) allows excluding possible systematic errors in the temperature evaluation.

To better understand the effect of the annealing on the cluster morphology and on the size distribution, bright-field (BFTEM) images of the sample have been taken *in-situ* after thermalization at each studied temperature. By comparing the images corresponding to as implanted samples (RT) and to 443 K, it is worth noting that even if melted (according to SAED analysis) the In clusters do no dissolve in the matrix
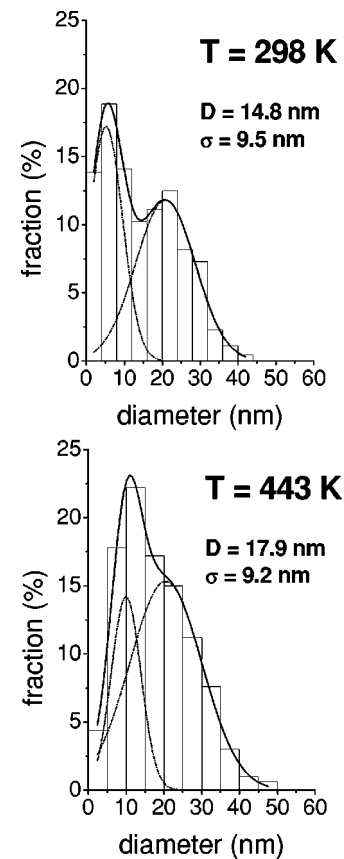

FIG. 4. Histograms of the size distributions of In clusters at 298 K (RT) and 443 K obtained from the Bright-Field TEM cross-section analysis.

after reaching the melting temperature. The shape of the clusters appeared to be spherical as concerns the smaller clusters and more droplike for the bigger ones located near the projected range of implantation. The corresponding histograms of the size distributions at RT and 443 K are shown in Fig. 4. The size was calculated as $\langle D \rangle = (a+b)/2$, where a and b are the major and minor axes of the droplike clusters. At RT, the distribution is bimodal with two components: one centered at about 5 nm and the other one at 20 nm, giving an average cluster size $\langle D \rangle_{RT} = 14.8$ nm and a standard deviation of the experimental distribution $\sigma_{RT} = 9.5$ nm. After the heating at 443 K, the centroid of the first component shifts from 5 nm to 10 nm, whereas the second one remains almost unaltered at 20 nm, resulting in an average cluster size $\langle D \rangle_{443\ K} = 17.9$ nm with $\sigma_{443\ K} = 9.2$ nm. This behavior can be interpreted as the onset of an Ostwald ripening regime[19] in which the smaller clusters melt, their In atoms diffuse in the matrix and increase the size of the larger clusters. It is worth stressing that the cluster size distribution obtained by TEM involves clusters either melted or crystalline.

To further investigate the observed stability of the In clusters above the melting temperature, the *in-situ* TEM experiment has been extended to annealing temperatures up to about 1000 K. The BFTEM results are reported in Fig. 5, which shows some representative BFTEM cross-sectional micrographs of the implanted sample collected during the thermal cycle from RT up to 983 K. Here, it is evident that
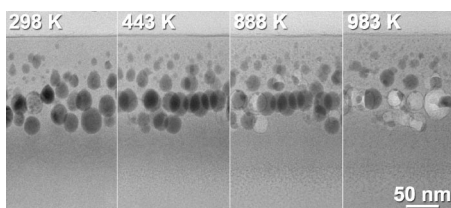
FIG. 5. Bright-Field TEM cross-sectional micrographs of the implanted sample collected at the following temperatures: 298 K (RT), 443 K, 888 K, and 983 K.
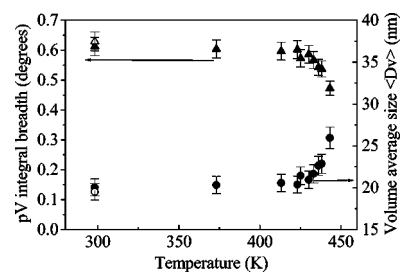

FIG. 6. Pseudo-Voigt integral breadth (solid triangles) of the In(101) GIXRD peak and the corresponding clusters volume averaged size $\langle D_V \rangle$ (solid circles) versus the temperature. The open symbols are referred to the measurements done at RT after the thermal annealing. The error bars are the estimated standard deviations (e.s.d.'s) obtained from the fit.

an exceptional thermal stability of the clusters which remain as a whole in their positions (even if completely molten and then amorphous) well beyond the In bulk melting point until a temperature of about 983 K, after that they progressively dissolved by leaving empty holes in the cross-sectioned matrix. The interpretation of such phenomenon is up to now not completely clear. A possible explanation could be the presence of a stable surface layer around the In clusters which prevents In atoms to diffuse in the matrix, like for instance a layer of indium oxide. For this layer to be visible in TEM imaging its thickness should be at least of the order of 1 nm. As no such layer is visible in the micrographs, a possible picture is that the surface In atoms are bounded to O atoms of the silica matrix, forming just one oxide monolayer. The formation enthalpy of In-In bond is 100 ± 8 kJ/mol which is less than that of In-O bond (320 ± 40 kJ/mol): this indicates a larger stability of the In-O bond with respect to the In-In one and that a higher temperature (about 800–900 K as estimated in the present case) is required for these surface In-O bonds to be thermally broken, allowing the underlying In atoms to diffuse inside the matrix. It is interesting to note that a similar temperature threshold is obtained in sequentially In+P implanted silica in which the formation of InP is obtained only after thermal annealing at temperature higher than 700 °C (973 K) at which In atoms are supposed to diffuse in the matrix to react with P atoms.[40]

In order to get more quantitative information about the thermodynamics of the In clusters near their melting, we have studied the x-ray diffraction peak shape as a function of the annealing temperature. A detailed peak shape analysis can be accomplished to all the In(101) reflections collected. According to this procedure, the diffraction peak was fitted iteratively by an analytical function to obtain line profile parameters defining the position, breadth, and shape of the Bragg reflection considered. Here, the diffraction line profiles were fitted by a pseudo-Voigt (pV) function (in practice, a sum of two pseudo-Voigt functions in order to take into account the $\alpha_1 - \alpha_2$ doublet) and it was assumed that the background in proximity of the reflection was parabolic. The position of the peak was also refined in order to obtain the interplanar distance $d_{(101)}$. Moreover, a correction function for peak asymmetry was considered and for all the investigated angular range the experimental data were corrected for polarization, Debye-Waller and Lorentz factors.

Assuming that all the inclusions have the same lattice parameter, we can determine the volume averaged crystallites size $\langle D_V \rangle$ from the total integral breadth of the simulated diffraction profiles by using Eqs. (4) and (5). Figure 6 shows

the pV integral breadth and the volume averaged crystallites size $\langle D_V \rangle$ during the heating sequence and after that, when the sample was recovered at RT. After an initial constant trend, the (101) In peak narrows rapidly and the volume average size $\langle D_V \rangle$ of the clusters increases with the temperature. At 423 K the average size of the clusters is 20.4 nm, after that temperature, the peak begins to reduce its integrated area and the average size increases until 26 nm at 443 K. After the melting, when the sample was cooled down to RT, the original average crystallite size was recovered (open circle and triangle in Fig. 6).

If we exclude the reorientation of the crystallites into a preferred orientation different from (101), the heating behavior of In clusters could be explained with a melting point dependence on the size of the clusters, according to which the smaller particles melt first than the bigger ones, as observed in the TEM analysis. As a consequence, the In clusters have a range of melting temperatures which corresponds roughly to the interval of variation of the In(101) integrated intensity. Therefore, when the solid-liquid transition begins, some clusters (the smallest) melt, the volume average size increases and the XRD integrated intensity decreases. According to XRD and TEM results (Figs. 2 and 3), the onset of the melting is at about 423 K which is 7 K below T_0 (melting point depression). On the other hand, the complete disappearance of the In(101) diffraction intensity would occur at the melting temperature of the last and largest crystallites in the sample. According to Figs. 2 and 3, the melting temperature of these largest particles is about 443 K which is 13 K above T_0. This means that the largest In clusters were superheated. Consequently, the observed increase of the average crystallite size with the temperature must be due to the crystallite size distribution shifting towards larger sizes as the smaller particles have melted.

In order to determine the crystallite size distribution, we fit the α_1 component of pseudo-Voigt functions obtained from line profile analysis with Eqs. (5) and (6) for a log normal distribution of diameters and approximately spherical clusters. Fitting parameters were the log normal mean γ and variance ω in Eq. (6), from which the crystallites diameter distributions can be reconstructed at each temperature investigated. The use of the log normal size distribution is justified by the fact that this distribution has proved to be appropriate
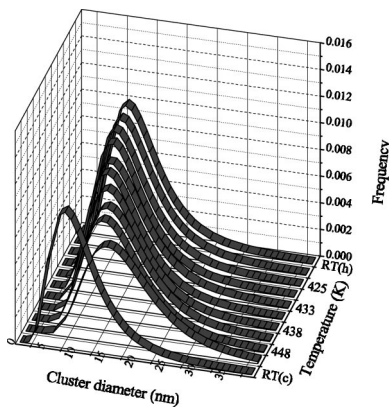
FIG. 7. Calculated diameters distributions of the In clusters versus the temperature. The clusters distributions were calculated by considering a log normal size distribution.

in most cases. As concerns the shape of the clusters, the assumption of an overall spherical form in the quantitative x-ray analysis is justified by the fact that we measured only one diffraction direction.

Figure 7 shows the calculated size distributions. Here, it is clear that the shifting of the crystallite size distributions is towards larger sizes with the temperature. This confirms the size-dependence melting point of the In nanoclusters.

V. THERMODYNAMIC MODEL

It is known that nanocrystals can exhibit both melting point depression and superheating depending on the size, interface and surface conditions of nanocrystals. Such phenomena can be illustrated by using thermodynamic considerations.

In the case of nanoclusters with a free surface, the relation between the cluster size and the melting temperature T_m can be predicted using a simple thermodynamic theory based on equating the Gibbs free energies of solid and liquid clusters and taking into account that the Gibbs energy of a small cluster has an additional term with respect to the bulk accounting for the free energy at the cluster surface. If we assume also that the clusters are spherical particles of diameter D and we neglect second-order terms, one obtain the following equation:[30]

$$\frac{T_0 - T_m(D)}{T_0} = \frac{4}{\rho_s LD}\left[\gamma_{sv} - \left(\frac{\rho_s}{\rho_l}\right)^{2/3}\gamma_{lv}\right], \qquad (8)$$

where T_0 is the equilibrium melting temperature of bulk solid, ρ_s is the solid phase density, ρ_l is the liquid phase density, L is the latent heat on melting, and γ_{sv} and γ_{lv} are the solid-vapor and liquid-vapor interfacial energies, respectively. This equation predicts the melting point depression of isolated clusters.

When nanocrystals are embedded in a matrix, the melting point can be enhanced depending principally on the interfacial relationship between matrix and cluster and secondarily the pressure given by the matrix on the cluster. From a thermodynamic point of view, the Gibbs energy of the embedded
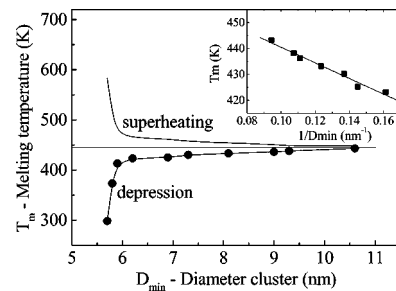

FIG. 8. Experimental melting temperature (solid circles) of the In clusters versus the diameter of the clusters. The solid line connecting the experimental points is only a guide for the eye. In the inset it is shown the linear fit of the higher temperature data corresponding to the melting interval.

cluster with respect to the isolated cluster has an additional term accounting for the cluster strain energy. Moreover, the term related to the cluster surface free energy can be strongly modified by the interface structural relationships between the cluster and the matrix. By using a similar thermodynamic approach, the relation between the cluster diameter D and the melting temperature $T_m(D)$ is the following:[41]

$$\frac{T_m(D) - T_0}{T_0} = \frac{1}{L}\left[\Delta E + \frac{6}{D}\left(\frac{\gamma_{lm}}{\rho_l} - \frac{\gamma_{sm}}{\rho_s}\right)\right], \qquad (9)$$

where γ_{lm} and γ_{sm} are the liquid and solid particle-matrix interfacial energies, respectively, ΔE is the strain energy difference resulting from the difference between the coefficients of thermal expansion of clusters and matrix and volume change on melting. From Eq. (13), we have

$$T_m(D) = \left(1 + \frac{\Delta E}{L}\right)T_0 + \frac{6T_0}{DL}\left(\frac{\gamma_{lm}}{\rho_l} - \frac{\gamma_{sm}}{\rho_s}\right). \qquad (10)$$

According to this equation, we have that at large diameters $T_m(D)$ tends asymptotically to the value $[1+(\Delta E/L)]T_0$ which is the bulk melting point corrected with the term $\Delta E/L$ accounting for the pressure variation on the clusters as a consequence of different matrix and cluster compressibility during the cluster volume increase (in general such correction enhances the melting point). At small diameters, the melting temperature can be higher or lower than the asymptotic value, according to the sign of $[(\gamma_{lm}/\rho_l) - (\gamma_{sm}/\rho_s)]$ which is closely related to the nature of the interface between the particle and the matrix: for clusters with coherent or semicoherent interfaces with the crystalline matrix the term is greater than 0 and large superheating can arise. In this case, the melting point increases inversely with the radius of the cluster. If no semicoherent interface exists (as in the present case, with an amorphous silica matrix) the term is less than 0 and melting point depression arises. In this case, the melting point decreases inversely with the radius of the cluster. The term ΔE generally may account only for a small contribution in the melting point elevation. The different trends of Eq. (10) are shown in Fig. 8 (solid lines). If the γ's and σ's are taken to be independent on temperature over the melting interval, T_m versus $1/D$ has a linear trend, according to Eq. (10).

To test this model with our experimental data, we need the pairs $(D; T_m(D))$, where $T_m(D)$ is the melting temperature of cluster with diameter D. On the other hand, we have the pairs $(\langle D \rangle; T_m(D))$ where $\langle D \rangle$ is the arithmetic mean size of the solid crystallites distribution at the temperature $T_m(D)$. In order to obtain such data pairs, we consider that at the temperature $T_m(D)$ the crystallite size distribution has a lower limit D_{min} which is very near to the size of the clusters which melt at that temperature. The value of D_{min} can be valued as $\langle D \rangle - \omega$, where ω is the standard deviation of the size distribution. Data obtained according to this description are depicted in Fig. 8 (solid circles). The experimental data clearly obey Eq. (10) with a melting point depression at small diameter and an asymptotic temperature higher than the In bulk melting point. The fit of the higher temperature data corresponding to the melting interval (shown in the inset) gives a slope of -301 ± 21 nm and an intercept of 470 ± 3 K, from which a superheating of 40 K was obtained. Moreover, the negative slope indicates absence of any coherence between the matrix-particle interfaces which is realistic by considering that the matrix is amorphous. Due to the difficulties in defining the pairs $(D; T_m(D))$, the values of slope and intercept are somewhat uncertain and have only the significance of verifying the theoretical model.

In conclusion, the experimental data are in good agreement with the model described by Eq. (10). The fit clearly shows that the melting point depression appears at small sizes and the superheating term is asymptotically reached as the clusters are so large that they can be treated as bulk. Such a behavior is the result of the combination of two effects: the thermodynamic size and the matrix pressure effects. Moreover, the significant supercooling observed is a consequence of the size of the precipitate: in order to start nucleation in a supercooled liquid, a nucleation grain of a certain size is needed and the minimum size for the nucleation decreases with increasing supercooling of the liquid.

Now, let us estimate the pressure on the clusters from their interplanar distance. The refined position of the x-ray Bragg peaks gives the interplanar distance d_{101} of the precipitates. The maximum excursion of the interplanar distance d_{101} during the thermal cycle was $\Delta d/d = 1.5 \times 10^{-3}$. By considering that the In isotropic bulk compressibility is 0.002 73 GPa^{-1}, then from the elasticity theory a hydrostatic pressure of -0.17 GPa was determined. From the Clausius-Clapeyron equation $dP/dT = L/T\Delta V$, where P is the pressure, T is the absolute melting temperature, L is the latent heat of fusion ($L = 3.25$ kJ/mol for In) and ΔV is the relative volume change during the melting ($\Delta V = 0.32$ cm^3/mol for In), we have that a pressure increase of 0.17 GPa during the melting enhances the melting temperature by 7 K. The result is in agreement with our experiments if we consider the uncertainty in the Bragg peak position determination.

VI. CONCLUSIONS

In this work, we investigated the thermal behavior of In nanoclusters embedded in silica obtained by ion implantation. This composite is an interesting system because it offers the possibility to easily investigate the melting-solidification phenomena in the case of nanometric clusters without a free surface and for the synthesis of In-based binary semiconductor compounds. The In precipitates were subjected to a heating-cooling cycle during which the microstructural properties of the clusters were studied by means of *in-situ* GIXRD and TEM.

A superheating of 13 ± 1 K and a supercooling of 107 ± 1 K for the embedded nanoclusters were found during the melting-solidifications cycles, evidencing the presence of a thermal hysteresis loop. A detailed study of the shape of the x-ray diffraction peak during the melting sequence indicates a melting point dependence on the size of the clusters according to which the smaller particles melt first than the bigger ones. The experimental results have been explained with a thermodynamic model which takes into account the combination of two effects: the thermodynamic size effect and the matrix pressure on the clusters. After the melting, the cluster remained stable as a whole in their positions in the form of liquid drops until a temperature of about 980 K, after that they progressively dissolved by leaving empty holes in the matrix. Several studies are in progress to investigate the reasons of the exceptional stability of the clusters well above the melting point.

---

*Author to whom the correspondence should be addressed. Email address: antonella.tagliente@brindisi.enea.it

[1] F. Gonella and P. Mazzoldi, *Handbook of Nanostructured Materials and Nanotechnology* (Academic, San Diego, 2000), Vol. 4: Optical Properties, Chap. 2, p. 81.

[2] J.L. Dormann, D. Fiorani, and E. Tronc, *Advances in Chemical Physics* (Wiley, New York, 1997), Vol. 283.

[3] M. Respaud, J.M. Broto, H. Rakoto, A.R. Fert, L. Thomas, B. Barbara, M. Verelst, E. Snoeck, P. Lecante, A. Mosset, J. Osuna, T. Ould Ely, C. Amiens, and B. Chaudret, Phys. Rev. B **57**, 2925 (1998).

[4] U. Kreibig and M. Vollmer, *Optical Properties of Metal Clusters* (Springer-Verlag, Berlin, Heidelberg, 1995).

[5] A.P. Alivisatos, Science **271**, 933 (1996).

[6] F. Yonezawa, S. Sakamoto, and F. Wooten, J. Non-Cryst. Solids **117–118**, 477 (1990).

[7] J. Zhao, X. Chen, and G. Wang, Phys. Rev. B **50**, 15 424 (1994).

[8] Da-ling Lu and Ken-ichi Tanaka, Phys. Rev. B **55**, 13 865 (1997).

[9] F. Tihay, G.M. Pourroy, A.C. Roger, and A. Kienneman, Appl. Catal., A **206**, 24 (2000).

[10] P. Mazzoldi, G.W. Arnold, G. Battaglin, F. Gonella, and R. Haglund, Jr., J. Nonlinear Opt. Phys. Mater. **5**, 285 (1996).

[11] C.W. White, J.D. Budai, S.P. Withrow, J.G. Zhu, E. Souder, R.A. Zuhr, A. Meldrum, D.M. Hembree, Jr., D.O. Henderson, and S. Prawer, Nucl. Instrum. Methods Phys. Res. B **141**, 228 (1998).

[12] E. Borsella, M.A. Garcia, G. Mattei, C. Maurizio, P. Mazzoldi, E. Cattaruzza, F. Gonella, G. Battaglin, A. Quaranta, and F. D'Acapito, J. Appl. Phys. **90**, 4467 (2001).

[13] L. Pavesi, L. Dal Negro, C. Mazzoleni, G. Franzo, and F. Priolo, Nature (London) **408**, 440 (2000).

[14] C.L. Chien, *Science and Technology of Nanostructures Magnetic Materials* (Plenum, New York, 1991), Vol. 259, p. 477.

[15] G. Battaglin, Nucl. Instrum. Methods Phys. Res. B **116**, 102 (1996).

[16] F. Gonella, Nucl. Instrum. Methods Phys. Res. B **166–167**, 831 (2000).

[17] G.W. Arnold and J.A. Borders, J. Appl. Phys. **48**, 1488 (1997).

[18] G. Mattei, Nucl. Instrum. Methods Phys. Res. B **191**, 323 (2002).

[19] A. Miotello, G. de Marchi, G. Mattei, P. Mazzoldi, and C. Sada, Phys. Rev. B **63**, 075409 (2001).

[20] G. De Marchi, G. Mattei, P. Mazzoldi, C. Sada, and A. Miotello, J. Appl. Phys. **92**, 4249 (2002).

[21] L. Gråbæk, J. Bohr, H.H. Andersen, A. Johansen, E. Johnson, L. Sarholt-Kristensen, and I.K. Robinson, Phys. Rev. B **45**, 2628 (1992).

[22] K.F. Peters, J.B. Cohen, and Y-W Chung, Phys. Rev. B **57**, 13 430 (1998).

[23] Q. Jiang, Z. Zhang, and J.C. Li, Chem. Phys. Lett. **322**, 549 (2000).

[24] Z.H. Jin, H.W. Sheng, and K. Lu, Phys. Rev. B **60**, 141 (1999).

[25] M. Zhang, M. Yu Efremov, F. Schiettekatte, E.A. Olson, A.T. Kwan, S.L. Lai, T. Wisleder, J.E. Greene, and L.H. Allen, Phys. Rev. B **62**, 10 548 (2000).

[26] M. Dippel, A. Maier, V. Gimple, H. Wider, W.E. Evenson, R.L. Rasera, and G. Schatz, Phys. Rev. Lett. **87**, 095505 (2001).

[27] G. Dybkjær, N. Kruse, A. Johansen, E. Johnson, L. Sarholt-Kristensen, and K.K. Bourdelle, Surf. Coat. Technol. **83**, 82 (1996).

[28] K.K. Nanda, S.N. Sahu, and S.N. Behera, Phys. Rev. A **66**, 013208 (2002).

[29] W.-H. Li, S.Y. Wu, C.C. Yang, S.K. Lai, K.C. Lee, H.L. Huang, and H.D. Yang, Phys. Rev. Lett. **89**, 135504 (2002).

[30] Ph. Buffat and J.-P. Borel, Phys. Rev. A **13**, 2287 (1976).

[31] R.W. Cahn, Nature (London) **323**, 668 (1986).

[32] H.W. Sheng, G. Ren, L.M. Peng, Z.Q. Hu, and K. Lu, Philos. Mag. Lett. **73**, 179 (1996).

[33] G.W. Greenwood, A.J.E. Foreman, and D.E. Rimmer, J. Nucl. Mater. **1**, 305 (1959).

[34] G.R. Carlow, Physica A **239**, 65 (1997).

[35] H. Trinkaus, Scr. Metall. **23**, 1773 (1989).

[36] L. G. Parrat, Phys. Rev. **95**, 359 (1954).

[37] A.J.C. Wilson, *X-ray Optics*, 2nd ed. (Methuen, London, 1962).

[38] J.I. Langford and A.J.C. Wilson, J. Appl. Crystallogr. **11**, 102 (1978).

[39] J.I. Langford, D. Louer, and P. Scardi, J. Appl. Crystallogr. **33**, 964 (2000).

[40] R. Mu, D.O. Henderson, Y.S. Tung, A. Ueda, C. Hall, W.E. Collins, C.W. White, R. A. Zhur, and J. G. Zhu, J. Vac. Sci. Technol. A **14**, 1482 (1996).

[41] P.R. Couchman and W.A. Jesser, Nature (London) **269**, 481 (1977).